



**HAL**  
open science

# Hydraulic conductivity, microstructure and texture of compacted claystone/ bentonite mixtures saturated with different solutions

M. Middelhoff, Olivier Cuisinier, Stéphane Gaboreau, F. Masrouri, J. Talandier, N. Michau

## ► To cite this version:

M. Middelhoff, Olivier Cuisinier, Stéphane Gaboreau, F. Masrouri, J. Talandier, et al.. Hydraulic conductivity, microstructure and texture of compacted claystone/ bentonite mixtures saturated with different solutions. *Applied Clay Science*, 2023, 241, pp.106982. 10.1016/j.clay.2023.106982 . hal-04119689

**HAL Id: hal-04119689**

**<https://hal.science/hal-04119689>**

Submitted on 6 Jun 2023

**HAL** is a multi-disciplinary open access archive for the deposit and dissemination of scientific research documents, whether they are published or not. The documents may come from teaching and research institutions in France or abroad, or from public or private research centers.

L'archive ouverte pluridisciplinaire **HAL**, est destinée au dépôt et à la diffusion de documents scientifiques de niveau recherche, publiés ou non, émanant des établissements d'enseignement et de recherche français ou étrangers, des laboratoires publics ou privés.

# 1 **Hydraulic conductivity, microstructure and texture of compacted claystone/** 2 **bentonite mixtures saturated with different solutions**

3 M. Middelhoff <sup>1,2 †</sup>, O. Cuisinier <sup>1\*</sup>, S. Gaboreau <sup>3</sup>, F. Masroui <sup>1</sup>, J. Talandier <sup>2</sup>, N. Michau <sup>2</sup>

4 <sup>1</sup> Université de Lorraine – LEMTA, UMR 7563 CNRS,  
5 (2 Rue du Doyen Marcel Roubault - BP 10162, 54000 Nancy CEDEX, France)

6 <sup>2</sup> Agence nationale pour la gestion des déchets radioactifs (Andra), France

7 <sup>3</sup> Bureau de recherches géologiques et minières (BRGM), France

8 [Olivier.Cuisinier@univ-lorraine.fr](mailto:Olivier.Cuisinier@univ-lorraine.fr)

9 Abstract: The French reference concept for the disposal of intermediate- and high-level nuclear waste  
10 in the Callovo-Oxfordian sedimentary rock formation (COX-claystone) considers the employment of  
11 crushed COX-claystone and its mixture with MX80-bentonite as potential backfill materials installed in  
12 drifts and shafts upon termination of the operational phase of the future repository. The fraction of  
13 MX80-bentonite in the mixture is limited to 30% in wet weight. Over time, the backfill will be saturated  
14 with solutions that originate in the surrounding rock formation and percolate through the concrete lining  
15 left in place. The main characteristic of the leachate will be its high pH-value. In addition to the swelling  
16 pressure, the sealing properties of the backfill are determined by the hydraulic conductivity. This labor-  
17 atory experimental study aimed to understand the hydraulic conductivity evolution of potential backfill  
18 materials under realistic conditions in terms of compaction conditions, solution chemistry, temperature  
19 and hydraulic gradient, and to relate results determined at the macroscale to results of microstructural  
20 and textural analysis. Also, the impact of the solution chemistry was evaluated by these means. In the  
21 case of mixture-samples, no stabilization of hydraulic conductivity was detected, despite the duration of  
22 the experiments being about one year. There was no detectable impact of the solution chemistry in the  
23 course of experiments attributable to low reaction kinetics under imposed conditions. Subsequent mi-  
24 crostructural analysis indicated material swelling triggering rearrangements in the pore space and low-  
25 ering the fraction of hydraulic conductive voids. Interestingly, neither the saturation nor the solution  
26 chemistry had an impact on the texture of materials.

27 **Keywords:** Callovo-Oxfordian claystone, MX80-bentonite, Hydraulic conductivity, Microstructure,  
28 Texture, Solution chemistry

29 † currently contracted by: Gesellschaft für Anlagen- und Reaktorsicherheit (GRS) gGmbH, Theodor-Heuss-Straße 4,  
38122 Braunschweig, Germany

## 30 1 Introduction and background

31 The French reference concept considers the disposal of intermediate and high level nu-  
32 clear waste in the Callovo-Oxfordian sedimentary rock formation located 500 m below ground  
33 level (ANDRA, 2005). Henceforth, the sedimentary rock formation is referred to as Callovo-  
34 Oxfordian (COX) claystone. The encapsulated nuclear waste will be emplaced in horizontal  
35 drifts, which will be sealed and backfilled once the operational phase of the repository is termi-  
36 nated. Unlike the seals, backfill is envisaged to be installed in situ by means of conventional  
37 compaction techniques. It will swell upon its saturation and inhibit the flow of fluid phases from  
38 the emplacement drifts to accessible biosphere over time. Its installation particularly aims to  
39 limit the propagation of the excavation damaged/ disturbed zone (EDZ/ EdZ) and to close the  
40 hydraulic conductive pore space (ANDRA, 2005). In addition to the swelling pressure evolving  
41 under the constant volume conditions, the hydraulic conductivity can be considered as one of  
42 the key parameters which govern the sealing properties of backfill.

43 Potential backfill materials are re-employed COX-claystone and its mixture with MX80-  
44 bentonite. COX-claystone is obtained during drift excavation and processed afterwards. Hence-  
45 forth, crushed and sieved COX-claystone is referred to as COX<sub>c</sub>. Its re-employment particularly  
46 aims to inhibit mineralogical and physico-chemical incompatibilities with the surrounding rock  
47 formation (ANDRA, 2005). A mixture composed of COX<sub>c</sub> and MX80-bentonite is considered  
48 alternatively, since the increased smectite fraction might enhance the barrier functions of back-  
49 fill. Like other smectite-containing materials, COX<sub>c</sub> and its mixture might be affected by var-  
50 iations in the material characteristics (e.g. textural and microstructural characteristics, initial  
51 dry density, degree of saturation etc.), the environmental conditions (e.g. solution chemistry  
52 etc.) and stress history (e.g. preconsolidation pressure, overburden pressure etc.) with regard to  
53 their hydro-mechanical behavior (e.g. Alonso et al., 1987; Chen, 1988). It must be thus evalu-  
54 ated whether the sealing characteristics of backfill are stable to possible variations over time.

55 According to Burland (1990), the structure of smectite-containing materials comprises  
56 fabric as well as interparticle bonding. Even though fabric also provides information about the  
57 arrangement of particles, this study adopts texture as it describes the features of particles (e.g.  
58 shape, orientation towards each other) and pores (e.g. shape, volume) more precisely.

59 Numerous laboratory experimental studies addressed the impact of the saturating solution  
60 chemistry on the physico-chemical and textural characteristics (e.g. Ramírez et al., 2005; Her-  
61 bert et al., 2008), the microstructure (e.g. Cuisinier et al., 2008; Fernández et al., 2014) and the  
62 hydro-mechanical behavior of smectite-containing materials (e.g. Villar, 2006; Karnland et al.,  
63 2007; Cuisinier et al., 2014; Zhang and Kröhn, 2019; Middelhoff et al., 2020). Considering the  
64 French reference concept, the impact of the pH is of major relevance, as described below.

65 Once the closure phase of the repository is terminated, the backfill might be saturated  
66 with solutions, which originate in the surrounding geological formation and percolate through  
67 the concrete lining left in place. The initial leachate is characterized by a pH above 13.5. This  
68 elevated pH is attributable to the release of potassium and sodium hydroxides from the concrete.  
69 After their leachate, the solution chemistry will be controlled by the dissolution of portlandite  
70 at a pH of 12.5 and later by the dissolution of cement phases at a pH ranging from 10.5 to 12.5.  
71 The phenomenon is referred to as hyperalkaline plume and might trigger different geochemical  
72 reactions while saturating the backfill (Huertas et al., 2000; Michau, 2005). Ion exchange at  
73 clay minerals can be expected once the alkaline solution percolates the backfill material. For  
74 instance, sodium ions can be replaced by calcium ions from the alkaline solution as their hy-  
75 dration potential is higher (Norrish, 1954). Simultaneously, the dissolution of clay minerals can  
76 be triggered as they remain relatively stable up to a pH of 9 and start dissolving once the pH  
77 exceeds 10. Secondary minerals, such as carbonates, clay minerals, cement phases, silicates,  
78 and zeolites, can precipitate or form afterwards. Their reaction kinetics and reaction mechanism  
79 are controlled by the pH of solutions, among other factors (Krauskopf, 1956). The analyses of

80 concrete lining/ claystone formation-interfaces sampled in situ indicated low reaction kinetics  
81 under real conditions (Gaboreau et al., 2011; Gaboreau et al., 2012). Thus, in order to determine  
82 a considerable impact of the solution chemistry on the backfill, the clay mineral/ pore water-  
83 system needs to remain thermodynamically unstable for a sufficiently long time.

84 To investigate the impact of the solution chemistry on the backfill materials in a reason-  
85 able period of time, most studies considered either simplified or extreme conditions, instead of  
86 realistic conditions. Simplified or extreme conditions comprise an increased liquid to solid ra-  
87 tio, an increased ionic strength of solutions, the employment of homoionic solutions and an  
88 increased temperature. In the case of hydraulic conductivity experiments, values can be pre-  
89 sumably obtained faster by imposing higher hydraulic gradients. However, there is no infor-  
90 mation about the impact of the magnitude of the hydraulic gradient on the reaction kinetics.

91 The impact of saturating solution chemistry on the physico-chemical and textural charac-  
92 teristics of smectite-containing materials is mainly investigated by conducting batch experi-  
93 ments characterized by a high liquid to solid ratio (e.g. Herbert et al., 2004; Hofmann et al.,  
94 2004; Ramírez et al., 2005; Fernández et al., 2014; Elert et al., 2015). However, there are sig-  
95 nificantly different results, particularly regarding the cation exchange capacity and specific sur-  
96 face area. Differences are attributable to the differences in the composition, ionic strength, and  
97 pH of solutions and in imposed temperatures. In general, results lack transferability to com-  
98 pacted materials predominantly due to the high liquid to solid ratio.

99 Micro-, meso- and macropores characterize the structure of compacted smectite-contain-  
100 ing materials in the unsaturated state and correspond to pores between clay particles, clay ag-  
101 gregates, and greater assemblies of clay aggregates and shielding grains, respectively. The ex-  
102 istence of meso- and macropores is indicated by a bi-modal pore-size distribution (PSD) which  
103 is commonly determined by means of mercury intrusion porosimetry (MIP) experiments

104 (Alonso et al., 1987). In addition, N<sub>2</sub>-gas sorption experiments are performed to provide further  
105 information, in particular on the existence of some smaller mesopores and micropores.

106         There are only a few studies addressing the impact of solution chemistry, in particular its  
107 pH, on the microstructure of compacted smectite-containing materials. For instance, the study  
108 of Cuisinier et al. (2008) comprised an aging process, in which compacted clayey soil samples  
109 were saturated with a portlandite-saturated solution (pH > 12) under elevated temperatures  
110 (> 50°C). The aging process lasted longer than 12 months. Subsequent MIP-experiments re-  
111 vealed that the macropores increased significantly, whereas the mesopores remained stable. The  
112 dissolution of smectite accounted for the increase in the amount of macropores, and might in  
113 turn provoke an increase in hydraulic conductivity (Romero, 2013). In general, the results are  
114 less transferable to compacted backfill materials, since the elevated temperatures accelerated  
115 the reaction kinetics and might have induced different reaction mechanisms.

116         There is a wealth of studies aiming to analyze the impact of saturating solution chemistry  
117 on the hydraulic conductivity behavior of compacted backfill materials under realistic condi-  
118 tions (e.g. Mata, 2003; Villar, 2006; Ye et al., 2014; Zhang and Kröhn, 2019; Zhang, 2021).  
119 Realistic conditions refer to the initial compaction conditions of samples, the saturating solution  
120 chemistry, and the ambient temperature. Their major conclusion was that the impact vanishes  
121 upon the ionic strength decreases or the dry density increases. Results were attributed to the  
122 modification of the pore size distribution and to the mobility of the water molecules within the  
123 macropores. However, interpretations were mainly based on diffuse double layer (DDL) theo-  
124 ries and thus lack direct experimental evidence.

125         Only a few studies related changes in the hydraulic conductivity behavior of smectite-  
126 containing materials to the impact of the saturating solution chemistry, in particular of the pH-  
127 value, on the physico-chemical and textural characteristics and microstructure (e.g. Pusch et al.,  
128 2003; Cuevas, 2005; Karnland et al., 2007; Cuisinier et al., 2014). Indeed, parts of the studies

129 of Pusch et al. (2003) and Cuevas (2005) were conducted under realistic conditions (e.g. com-  
130 paction state, solution chemistry, ambient temperature) and are thus of special interest. How-  
131 ever, both studies lacked completeness as they disregarded the microstructure and attributed  
132 changes in the hydraulic conductivity to the impact of the solution chemistry on the physico-  
133 chemical and textural characteristics only. Results indicated that the solution chemistry affected  
134 neither the hydraulic conductivity of materials nor their cation exchange capacity and specific  
135 surface area. Those observations were attributed to the low reaction kinetics. Despite the con-  
136 clusion, the sealing properties of potential backfill materials were assumed to be long-term sta-  
137 ble to the saturating solution chemistry under realistic conditions.

138         The literature review revealed that compared to the one-dimensional volume change be-  
139 havior (e.g. compressibility, swelling pressure) the fluid transfer behavior of COX<sub>c</sub>-based ma-  
140 terials was little investigated although it determines the sealing behavior of the backfill. Former  
141 experiment programs also disregarded relevant boundary conditions, in particular the pH-value  
142 of saturating solutions. This study thus aims to determine the hydraulic conductivity of COX<sub>c</sub>  
143 and its mixture with MX80-bentonite by means of constant-head experiments, whose condi-  
144 tions were believed to induce repository-like conditions in terms of compaction state, tempera-  
145 ture, hydraulic gradient and solution chemistry. Subsequent N<sub>2</sub>-gas sorption and mercury intru-  
146 sion porosimetry (MIP) experiments serve the purpose of linking differences in the hydraulic  
147 conductivity to changes in the texture and microstructure of materials. In particular, the satura-  
148 tion of materials with a hyperalkaline solution is expected to induce considerable changes. The  
149 analyse of the spatial distribution of textural and microstructural parameters allow to assess  
150 whether the hydraulic conductivity is still evolving in the short- and intermediate-term or re-  
151 flects a long-term stable state. The experimental program involving the saturation of materials  
152 with a hyperalkaline solution and the approach of linking directly the evolution of hydraulic  
153 conductivity to textural and microstructural changes constitute the uniqueness of this study.

## 154 2 Materials

155 The materials investigated were COX<sub>c</sub> and its mixture with MX80-bentonite (Wyoming,  
156 USA). The mixture was composed of 70% COX<sub>c</sub> and 30% MX80-bentonite in wet weight. The  
157 limitation of MX80-bentonite to 30% was based on the reasons mentioned above (e.g. reduc-  
158 tions of incompatibilities with the surrounding formation). COX-claystone was obtained during  
159 the excavation of drifts of Andra's URL in a depth of – 490 m (Bure, Meuse/ Haute-Marne  
160 region, France). Conil et al. (2018) highlighted that the mineralogical composition, water con-  
161 tent and porosity of intact COX-claystone samples vary with their position in the rock for-  
162 mation. Correspondingly, COX<sub>c</sub> was expected to consist of about 46% phyllosilicates (e.g. ill-  
163 lite, ordered illite/ smectite mixed layer minerals), 24% tectosilicates (e.g. quartz, feldspars),  
164 27% carbonates (e.g. calcite, dolomite), and minor fractions of associated minerals (e.g. pyrite).  
165 In accordance with the reference concept, the subsequent processing of material comprised the  
166 crushing and sieving to a maximum grain size of 2 mm. The material was then stored in airtight  
167 containers. The wealth of information about the volume change, transfer, and sorption behavior  
168 of MX80-bentonite accounted for its selection to be mixed with COX<sub>c</sub>. MX80-bentonite was  
169 supplied by Laviosa-MPC SAS (Limay, France), who already processed the material to a max-  
170 imum grain size of 2 mm before filling it in airtight containers. It is noteworthy that the supplier  
171 indeed sells its bentonite from Wyoming under the commercial name of Expangel SP7, but it  
172 is commonly identified under the name of MX80. Its mineralogical composition is dominated  
173 by phyllosilicates (e.g. smectites), whose fraction is about 80%. Other minerals are tectosili-  
174 cates (e.g. quartz, feldspars) and carbonates (e.g. calcite) (e.g. Molinero-Guerra et al., 2020).

175 Information about the physical and physico-chemical characteristics of COX<sub>c</sub> and its mix-  
176 ture with bentonite are given in Table 1. Physical characteristics of COX<sub>c</sub> and its mixture with  
177 MX80-bentonite were taken from Middelhoff et al. (2020). The external specific surface area  
178 (SSA) and the cation exchange capacity (CEC) of COX<sub>c</sub> and the mixture were determined by



179 means of the BET- and cobalt hexamine methods (Orsini and Remy, 1976), respectively. The  
180 latter was also employed to determine the exchangeable cation species. Values of SSA and CEC  
181 of COX<sub>c</sub> were in good agreement with previous studies (Gaucher et al., 2004; Yven et al., 2007).  
182 The dominant exchangeable cation species in COX<sub>c</sub> were Ca<sup>2+</sup>, Mg<sup>2+</sup>, Na<sup>+</sup> and K<sup>+</sup>, listed ac-  
183 cording to their amount encountered. Corresponding amounts were 53%, 21%, 13% and 12%  
184 of adsorbed cations, respectively. The replacement of COX<sub>c</sub> by 30% MX80-bentonite led to a  
185 significant increase in the fraction of Na<sup>+</sup>-ions. The exchangeable cations were then dominated  
186 by Na<sup>+</sup>-ions, followed by Ca<sup>2+</sup>-, Mg<sup>2+</sup>- and K<sup>+</sup>-ions with respect to their amount. Corresponding  
187 amounts were 43%, 36%, 15% and 6% of adsorbed cations, respectively.

188         The grain size distribution curves of COX<sub>c</sub> and the mixture are shown in Figure 1. The  
189 size distribution of grains smaller than 0.8 mm was measured by means of laser diffractometry  
190 (ISO, 2009), whereas dry sieving was conducted in order to obtain the size distribution of the  
191 residual grains. As depicted, the distribution curves of both materials were comparable. The  
192 compaction behavior of both materials was investigated by means of standard and modified  
193 Proctor experiments. Materials were prepared at various water contents by adding correspond-  
194 ing quantities of deaired/ demineralized water. They were left in airtight containers for more  
195 than one week occasionally revolved to guarantee the homogeneous distribution of added water.  
196 A detailed description of results of standard and modified Proctor experiments and their inter-  
197 pretation are given in Middelhoff et al. (2020). Modified Proctor experiments revealed that the  
198 maximum dry density and optimum water content were 1.95 Mg/m<sup>3</sup> and 13.2%, respectively,  
199 in the case of COX<sub>c</sub>, and 1.72 Mg/m<sup>3</sup> and 18.2%, respectively, in the case of the mixture.

200         The laboratory experimental program comprised the saturation of both materials with  
201 three solutions differing in their composition and properties. Deaired/ demineralized water  
202 served as a reference solution. Henceforth, water referred to deaired/ demineralized water, and  
203 the subscripts SS and AS indicated the artificial site solution and the artificial alkaline solution,

204 respectively. The compositions of the site and alkaline solution corresponded to the rock for-  
205 mation water and to solutions believed to evolve from percolating through the concrete lining,  
206 respectively. Both solutions were prepared according to a protocol established and provided by  
207 Andra (Middelhoff et al., 2020). Their compositions and key properties are given in Table 2.  
208 The site and the alkaline solutions were comparable in terms of the order of magnitude of their  
209 ionic strength, however the alkaline solution was characterized by an elevated pH. The pH of  
210 AS corresponded to the solution chemistry controlled by the dissolution of portlandite.

## 211 3 Experiments

212 The hydraulic conductivity, microstructure and texture of COX<sub>c</sub> and its mixture with  
213 MX80-bentonite were determined by means of constant head experiments, mercury intrusion  
214 porosimetry (MIP) experiments and N<sub>2</sub>-gas sorption experiments, respectively. The sample  
215 preparation, experiment protocols adopted, and the program established are described below.

### 216 3.1 Sample preparation

217 Materials were prepared according to the protocol presented in section 0. Samples were  
218 then compacted to the maximum dry density at the optimum water content by means of the  
219 static compaction method at a controlled deformation rate of 0.1 mm/s. The protocol envisaged  
220 the compaction of materials directly inside the mold in order to reduce the risk of the develop-  
221 ment of preferential paths along the sample/mold-interface. The initial height and diameter of  
222 all samples were 30 mm and 70 mm, respectively. Information about the initial characteristics  
223 of COX<sub>c</sub> and mixture-samples is given in Table 3.

224 In the case of the mixture-samples, the microstructural and textural analyses were per-  
225 formed shortly after the termination of the hydraulic conductivity experiments. Before they  
226 were analyzed, samples were cut perpendicularly to their center axis into discs of same height.  
227 The center axis corresponded to the imposed flow direction. The purpose of this preparation

228 step was to determine the possible spatial evolution of the microstructure and texture triggered  
229 by the saturation and the solution chemistry. Supplementary COX<sub>c</sub>- and mixture-samples were  
230 prepared in the same way to evaluate the impact of the partial material replacement and to  
231 compare the structure of material before and after saturation.

### 232 3.2 Hydraulic conductivity experiments

233 The setup of hydraulic conductivity experiments is depicted in Figure 2. The employed  
234 constant-volume hydraulic conductivity cell (rigid wall permeameter) was composed of its  
235 mold, two porous discs, its lid, and its bottom plate. The latter two included one o-ring each.  
236 The mold containing the sample was sandwiched between the porous discs. This assembly was  
237 then placed between the lid and the bottom part, which were finally screwed together.

238 The constant head method was considered to be most adequate to investigate the hydrau-  
239 lic conductivity of both samples (e.g. Dixon et al., 1999; Mata and Ledesma, 2003; Villar,  
240 2006). By means of a constant volume/ pressure control unit, samples were saturated from the  
241 bottom upwards. Solutions left the cell at its top and were finally collected in a graduated flask.  
242 The accuracy of the measurement of outflow was about 0.5 mL. In order to avoid interaction  
243 processes of the solution with the atmosphere (e.g. evaporation, exchange of CO<sub>2</sub>), the flask  
244 was plugged, allowing only solutions to enter. The increase of gas pressure inside the flask was  
245 expected to be negligible.

246 Imposed injection pressures increased stepwise from 15 kPa to 90 kPa in the first weeks  
247 of the experiments. Considering a sample height of 30 mm, corresponding hydraulic gradients  
248 varied from 50 m/m to 300 m/m, which reflected the conditions encountered in situ. The pore  
249 pressure measured in undisturbed COX-claystone varies from 4,000 to 5,000 kPa (Seyedi et al.,  
250 2017). Assuming atmospheric pressure in the drift and a minimum extension of the EdZ of  
251 about 8 m, the corresponding hydraulic gradient varies from 50 m/m to 60 m/m. Hydraulic  
252 gradients that were imposed in this experiment program were still higher since there was a need

253 to accelerate the experiments. The minimum volume injected was equal to two times of the  
254 initial pore volume of the sample.

255 Hydraulic conductivity experiments were performed under an ambient temperature of  
256 22°C. The temperature was in accordance with the results of Tourchi et al. (2021), who repro-  
257 duced a full-scale in situ heating experiment in COX-claystone by performing numerical sim-  
258 ulations. Their simulations revealed that the temperature at the edge of the access galleries  
259 would not exceed 23°C after waste emplacement.

### 260 3.3 Microstructural analysis

261 Mercury intrusion porosimetry (MIP) experiments were conducted by means of an Auto-  
262 Pore IV 9500 apparatus (Micromeritics, U.S.A.). Prior to the microstructural analysis, samples  
263 were outgassed under a residual pressure of  $1.6 \times 10^{-6}$  Pa at a temperature of 80°C for 24 hours.  
264 The residual pressure involves the condensation of pore water at lower temperatures and, in  
265 turn, negligible shrinkage. Gaboreau et al. (2016) evaluated different pre-treatment methods for  
266 microstructural analysis and showed that the method adopted yields coherent results.

267 The MIP-method bases on the principle of forcing a non-wetting fluid, like mercury, to  
268 enter a porous medium by incrementally increasing injection pressures. Detailed information  
269 about its principle and procedure are given in Cuisinier and Laloui (2004) and Delage et al.  
270 (2006), for instance. The result of MIP-experiments is the cumulative volume of mercury in-  
271 truded as a function of the equivalent pore diameter. The pore size distribution (PSD) curve is  
272 deduced from those results in order to facilitate their interpretation (Juang and Holtz, 1986). It  
273 is defined as the derivative of the total volume of mercury intruded with respect to the common  
274 logarithm of the equivalent pore diameter. In this study, the approach of PSD-curve determina-  
275 tion followed that presented by Juang and Holtz (1986) and used a constant value of  $\Delta(\log(d_i))$   
276 being equal to 0.25. The determination of PSD by means of MIP is limited, regarding the intru-

277 sion of pores, whose diameter are smaller and larger than 7 nm and 600 nm, respectively. Re-  
278 sults might also be impaired through the occurrence of the bottleneck phenomenon or pore  
279 entrapment, for instance (e.g. Romero et al., 1999; Delage et al., 2006; Romero, 2013).

### 280 3.4 Textural analysis

281 Nitrogen gas (N<sub>2</sub>) adsorption-desorption cycles were determined by means of an ASAP  
282 2050 volumetric adsorption analyzer (Micromeritics, U.S.A.) at 77K. Block samples were ini-  
283 tially outgassed under a residual pressure of  $1.6 \times 10^{-6}$  Pa at 80°C. The outgassing lasted 24  
284 hours. The nitrogen gas adsorption method adopts the physical adsorption of non-reactive gas  
285 molecules, like nitrogen, on solid external surfaces. Information about its principle and proce-  
286 dure is given in Gregg and Sing (1982), for instance. BET theory and a generalized *t*-plot  
287 method were adopted to describe the texture of solids (Lippens and Boer, 1965).

### 288 3.5 Pore classification

289 The diameter of macropores is larger than  $5 \times 10^1$  nm, whereas the diameter of mesopores  
290 ranges between  $2 \times 10^0$  nm and  $5 \times 10^1$  nm. Micropores are characterized by a diameter smaller  
291 than  $2 \times 10^0$  nm (e.g. Thommes et al., 2015). In this study, the lower limit of the class of meso-  
292 pores was shifted to the entrance pore diameter of  $7 \times 10^0$  nm, since the mesopores, whose di-  
293 ameters are smaller than  $7 \times 10^0$  nm, cannot be detected by means of the MIP method. The range  
294 of the class of mesopores was accordingly reduced by 10% and the bias was expected to be  
295 negligible in the further interpretation of results.

### 296 3.6 Experimental program

297 The program comprised four samples of COX<sub>c</sub> and four samples of the mixture, respec-  
298 tively indicated by the prefix C and M in their sample identification. The suffix I, W, SS and  
299 AS referred to samples analyzed in their initial state, and to samples analyzed during/ after the

300 saturation with water, site solution and alkaline solution, respectively. The detailed experiment  
301 program is given in Table 4. In terms of structural alterations, M-SS and M-AS were expected  
302 to react most considerably to the saturation with different solutions due to their elevated smec-  
303 tite fraction and particular solution chemistry. Therefore, they were selected for the subsequent  
304 microstructural and textural analysis. This approach provided the basis to evaluate the impact  
305 of the saturation process and saturating solution chemistry on the material properties.

## 306 4 Results

307 In this section, the results obtained in the hydraulic conductivity experiments are pre-  
308 sented first, followed by the results of subsequent microstructural and textural analysis. The  
309 presentation reflects the sequence of data acquisition.

### 310 4.1 Hydraulic conductivity experiments

311 Values of hydraulic conductivity were determined upon the establishment of steady state  
312 condition (hydraulic equilibrium) that was indicated by stabilized rates of inflow and outflow  
313 of solutions. Moreover, the hydraulic equilibrium implied full saturation of samples. Both ma-  
314 terials were saturated with water, the site and alkaline solution. The normalized volume of in-  
315 flow and the hydraulic conductivity of  $COX_c$  are plotted against the normalized volume of out-  
316 flow in Figure 3a and c, respectively, whereas Figure 3b and d depict the evolution of the nor-  
317 malized volume of inflow and hydraulic conductivity of the mixture as a function of the nor-  
318 malized volume of outflow. The normalized volume of inflow and outflow are the ratios of  
319 volume of measured inflow and outflow, respectively, to the initial pore volume and serves the  
320 purpose of emphasizing the amount of pore solution exchanged. Data obtained were subse-  
321 quently processed by means of a moving average method.

322 Focusing on  $COX_c$ , inflow rates increased once the hydraulic gradient was raised stepwise  
323 and stabilized. The inflow volume ranged from the threefold to the fivefold of the initial pore

324 volume. The greatest volume of solution was injected into C-AS. In all three experiments, the  
325 onset of outflow was determined once the volume of solution corresponding to one initial pore  
326 volume was injected into the samples. Shortly after the onset of outflow was detected, steady  
327 state conditions established at an average flow rate ranging from 2 mL/day to 2.5 mL/ day. The  
328 former rate refers to C-W. As depicted in Figure 3a and c, pore solution was exchanged at least  
329 twice within a period of about 60 days. The smallest number of exchanges was exhibited by  
330 C-W, which corresponded to the smaller average flow rates. In the course of the experiments,  
331 values of hydraulic conductivity calculated decreased initially and stabilized at values between  
332  $6 \times 10^{-11}$  m/s to  $9 \times 10^{-11}$  m/s. Samples C-SS and C-AS exhibited slightly higher hydraulic con-  
333 ductivities than C-W.

334 Total inflow volume into mixture-samples varied from the twofold to the threefold of the  
335 initial pore volume and were thus less than that injected into  $\text{COX}_c$ -samples, despite the fact  
336 that the experiments lasted five to six times longer (300 days – 360 days). In the case of M-W  
337 and M-SS, outflow was detected after injecting the volume of solution corresponding to one  
338 initial pore volume. In the case of M-AS, the volume of solution corresponding to two initial  
339 pore volumes were injected prior to the onset of outflow that might be attributable to a greater  
340 amount of air in the porous disc of the bottom plate. Indeed, steady state conditions were estab-  
341 lished shortly after detecting an outflow. However, the inflow and outflow rates decreased  
342 steadily in the course of the experiments, starting from 0.4 mL/ day at the beginning to 0.2 mL/  
343 days in the end. The trend is also identifiable in Figure 3d. Values of hydraulic conductivity  
344 accordingly decreased from  $2 \times 10^{-11}$  m/s to  $3 \times 10^{-12}$  m/s. Comparing the values of hydraulic con-  
345 ductivity at the same normalized outflow of 0.6, M-AS exhibited the smallest values.

346 The hydraulic conductivity of  $\text{COX}_c$  was by one order of magnitude higher than that of  
347 the mixture. The difference became even more considerable as the values of  $\text{COX}_c$  stabilized,  
348 whereas the values of the mixture progressively decreased in the course of the experiment.

349 Apart from that, the chemistry of the site and alkaline solution had no considerable impact on  
350 the hydraulic conductivity of both materials. The characterization of the microstructure and  
351 texture was of special interest at this stage, in order to evaluate whether the evolution at mac-  
352 roscales was reflected in the material properties at the nano- and microscale.

## 353 4.2 Microstructural analysis

354 Samples were prepared by cutting them perpendicularly to their center axis into two discs  
355 of same height (15 mm) in the case of MIP experiments. Henceforth, top part (T) and bottom  
356 part (B) referred to the upper part and lower part of the initial sample, respectively. Results of  
357 MIP-experiments performed on C-I, M-I, M-SS and M-AS are depicted in Figure 4.

358 In general, the quantities of micropores, mesopores and macropores are expressed as mi-  
359 cro-void ratio ( $e_\mu$ ), meso-void ratio ( $e_m$ ) and macro-void ratio ( $e_M$ ), respectively. The cumulative  
360 void ratio was calculated as the ratio of the cumulated volume of mercury intruded in voids to  
361 the volume of solids. The micro-void ratio was defined as the difference between the total void  
362 ratio ( $e_{Tot}$ ) and the sum of the meso-void ratio and the macro-void ratio. Since the porosity ( $n$ )  
363 of top and bottom parts of each sample was also measured in MIP-experiments, the total void  
364 ratio ( $e_{Tot}$ ) was calculated as the ratio of porosity to the difference of 1 to porosity. The approach  
365 was exemplified by the top parts of samples in Figure 4. Complementing Figure 4, Table 5  
366 provides absolute and relative values of micro-, meso-, and macro-void ratios. It facilitates the  
367 evaluation of the impact of partial replacement of COX<sub>c</sub> by MX80-bentonite, saturation and  
368 solution chemistry. Relative values were defined as the ratios of micro-, meso-, and macro-void  
369 ratio to the total void ratio of the corresponding sample part (= normalization) and are provided  
370 in order to disregard the impact of initial dry density, in particular on the macro-void ratios.

371 In the case of C-I, the volume of pores appeared to reduce along the center axis of the  
372 sample since the cumulative volume of mercury intruded in C-I (T) was higher than that of  
373 C-I (B). In the case of M-I, the opposite was observed. A distinct double peak was revealed by



374 the pore size distribution curves in the upper parts of Figure 4. It indicated the existence of  
375 meso- and macropores. As depicted in Figure 4a, the peaks of meso- and macropores of C-I (T)  
376 and C-I (B) occurred at the same pore diameter of about  $4 \times 10^1$  nm and  $2.5 \times 10^4$  nm, respec-  
377 tively. The comparison of relative meso- and macro-void ratios of C-I (T) to those of C-I (B)  
378 revealed similar values. M-I (T) was characterized by meso- and macropores at pore diameters  
379 of about  $3 \times 10^1$  nm and  $5 \times 10^4$  nm, respectively (Figure 4c). Meso- and macropores of M-I (B)  
380 occurred at pore diameters of about  $4 \times 10^1$  nm and  $2.5 \times 10^4$  nm, respectively. The relative meso-  
381 void ratio of M-I (T) was 5% higher than that of M-I (B), whereas the relative macro-void ratio  
382 of M-I (T) was 8% lower than that of M-I (B).

383 As highlighted in the lower parts of Figure 4 and in Table 5, the microstructure of M-SS  
384 and M-AS evolved comparably, despite they were saturated with different solutions. Top parts  
385 of M-SS and M-AS were characterized by the majority of mesopores occurring at a diameter  
386 of  $2.5 \times 10^1$  nm. Compared to those of M-I (T), relative meso-void ratios of M-SS (T) and  
387 M-AS (T) increased by 7% and 9%, respectively. The majority of macropores was determined  
388 at a diameter of  $4 \times 10^4$  nm in the cases of M-I (T) and M-AS (T), and at a diameter of  $2 \times 10^4$  nm  
389 in the case of M-SS (T). The comparison of the relative macro-void ratio of M-I (T) to those of  
390 M-SS (T) and M-AS (T) revealed similar values. M-AS (B) was characterized by a mesopore  
391 diameter of  $2 \times 10^1$  nm, whereas the mesopores of M-SS (B) occurred at  $4 \times 10^1$  nm. Relative  
392 meso-void ratios of both M-SS (B) and M-AS (B) were increased by about 8% and 15%, re-  
393 spectively, when they are compared to M-I (B). Bottom parts of mixture samples were charac-  
394 terized by the majority of macropores occurring at a diameter of  $2 \times 10^4$  nm. Interestingly, an  
395 additional macropore population was determined at diameters of  $8 \times 10^4$  nm in the case of  
396 M-SS (B). Compared to those of M-I (B), relative macro-void ratios of M-SS (B) and M-AS (B)  
397 reduced by about 9% and 6%, respectively.

398           The similar relative micro-, meso- and macro-void ratios of C-I and M-I accounted for  
399 the fact that the impact of the partial replacement of COX<sub>c</sub> by MX80-bentonite remained un-  
400 clear yet. Unlike the solution chemistry, the saturation had an impact on the microstructure of  
401 samples since the relative micro- and macro-void ratios decreased and aligned with each other,  
402 and the relative meso-void ratios increased.

### 403 4.3 Textural analysis

404           In the case of textural analysis, sample preparation involved to cut samples perpendicu-  
405 larly to their center axis into three discs of same height (10 mm) in order to identify possible  
406 spatial variations in the N<sub>2</sub>-gas sorption isotherms and the external specific surface area (SSA)  
407 along the flow direction. Henceforth, top part (Top), middle part (Middle) and bottom part  
408 (Bottom) referred to the upper, middle and lower parts of the initial sample, respectively. Sorp-  
409 tion isotherms determined by means of the N<sub>2</sub>-gas sorption method are depicted in Figure 5.

410           Isotherms displayed a Type II behavior and a H3 hysteresis loop. The reversible Type II  
411 isotherm is the normal form of isotherm obtained with a macroporous adsorbent. The Type II  
412 represents unrestricted multilayer adsorption build up and the occurrence of mesopores. The  
413 Type H3 loop not exhibiting any limited adsorption at high P/P<sub>0</sub>-ratios was coherent with ag-  
414 gregates of plate-like particles. It gave rise to slit-shaped pores and proved that the samples  
415 were mesoporous. Isotherms gave linear BET plots from 0.04 to 0.4 P/P<sub>0</sub> for all tested samples.

416           SSA-values obtained by means of BET- and *t*-plot-method are compiled in Table 6. Cal-  
417 culated BET specific surface areas (*S*<sub>BET</sub>) and associated monolayer capacity (*V*<sub>*m*</sub>) exhibited  
418 neither variations in SSA among mixture-samples, nor an evolution of SSA over the length of  
419 the individual samples. *t*-plot results were coherent with the *S*<sub>BET</sub>- values.

## 420 5 Discussion

421 The study aimed to understand the evolution of hydraulic conductivity of COX<sub>c</sub> and its  
422 mixture with MX80-bentonite under quasi-realistic conditions by relating the results obtained  
423 at the macroscale to those obtained at the microscale. Quasi-realistic conditions refer to the fact  
424 that the compaction conditions, solution chemistry, ambient temperature and hydraulic gradient  
425 were believed to be in a realistic range. Since the saturation itself as well as the saturation with  
426 solutions of different chemistry affected the materials in more or less pronounced manner, it  
427 appeared to be suitable to arrange the discussion accordingly.

### 428 5.1 Impact of saturation

429 The existence of meso- and macropores in COX<sub>c</sub> and its mixture with MX80-bentonite  
430 was indicated by bi-modal PSD-curves. This finding was consistent with the literature as smec-  
431 tite-containing materials are usually characterized by such a double-structure if they are com-  
432 pacted at the dry side of optimum water content (Alonso et al., 1987).

433 Highlighted in Table 5, the void ratio of M-I (T) was lower than that of M-I (B). The  
434 density gradient was induced by the static compaction method and ensued as a shear stress  
435 evolved at the interface between the material and mold (e.g. Villar, 2006). The decrease in  
436 initial dry density raised the total pore volume, in particular the macropore volume. This finding  
437 was consistent with the literature (e.g. Lloret and Villar, 2007). Interestingly, the static com-  
438 paction method had no impact on the distribution of pores in C-I (T) and C-I (B), although its  
439 water content was smaller than that of M-I. As a consequence, the evolution of higher shear  
440 stresses and a density gradient was expected.

441 The normalization of void ratios allowed to disregard the impact of densification on the  
442 microstructure of C-I and M-I and to evaluate quantitatively the impact of the partial replace-  
443 ment of COX<sub>c</sub> by MX80-bentonite. The comparison of C-I to M-I indicated that M-I indeed  
444 incorporated more macro-pores but less meso-pores on average. The average micro-void ratios

445 of C-I and M-I were comparable (Table 5). Apparently, the higher macro-void ratio of M-I  
446 ensued as the higher amount of smectite particles provoked the formation of more card-house-  
447 like aggregates, including more inter-aggregate pores.

448 The saturation of M-SS and M-AS led to a decrease in macro-void ratios and to an in-  
449 crease in micro- and meso-void ratios. Small differences along the center axis likely indicated  
450 a homogeneous saturation of samples. The decrease in macro-void ratio was attributable to the  
451 closure of hydraulic conductive pores ensuing as smectite particles and aggregates swell and  
452 rearrange upon saturation (e.g. Komine, 2004, 2010).

453 Information about COX<sub>c</sub> and its mixtures with MX80-bentonite, in particular their one-  
454 dimensional compression and swelling behavior under saturation, is given by Tang et al. (2010),  
455 Wang et al. (2012), Zeng et al. (2019), Middelhoff et al. (2020) and Robinet et al. (2021), for  
456 instance. In contrast, their hydraulic conductivity behavior under saturation was less intensely  
457 analyzed. The studies of Zhang and Kröhn (2019) and Zhang (2021) were thus of major interest  
458 since they determined the saturated hydraulic conductivity of compacted COX<sub>c</sub> and different  
459 COX<sub>c</sub>/ MX80-bentonite-mixtures, among other hydro-mechanical parameters. Prior to testing,  
460 all samples of Zhang and Kröhn (2019) were prepared to target dry densities of about 2.0 Mg/m<sup>3</sup>  
461 at initial water contents of about 4%. The corresponding total void ratios were about 0.33. In  
462 the case of COX<sub>c</sub>, values of hydraulic conductivity were about  $5 \times 10^{-13}$  m/s and assumed to  
463 reflect a long-term stable state. Tang et al. (2010) also focused on the saturated hydraulic con-  
464 ductivity of COX<sub>c</sub>, whose initial water contents ranged between 2% to 8%. Target dry densities  
465 were also about 2.0 Mg/m<sup>3</sup>. They determined a saturated hydraulic conductivity of about  $3 \times 10^{-12}$   
466 m/s. Moreover, their results indicated to a negligible impact of the initial water content on  
467 the hydraulic conductivity. The one and two orders of magnitude lower saturated hydraulic  
468 conductivities of Tang et al. (2010) and Zhang and Kröhn (2019) were attributable to the lower  
469 initial dry densities and/ or higher initial total void ratios of C-SS and C-AS most probably

470 (Table 5). In the case of a mixture that was composed of 80% COX<sub>c</sub> and 20% MX80-bentonite  
471 in weight, Zhang and Kröhn (2019) measured values of saturated hydraulic conductivities var-  
472 ying from  $1 \times 10^{-12}$  m/s to  $2 \times 10^{-12}$  m/s. Their values were in good agreement with the values  
473 obtained for M-SS and M-AS. Considering the initial compaction conditions, the recent results  
474 were remarkable since Zhang and Kröhn (2019) and Zhang (2021) compacted mixture samples  
475 to higher initial dry densities at lower initial water content with higher compaction energy be-  
476 fore they performed hydraulic conductivity experiments. Nevertheless, the magnitude of satu-  
477 rated hydraulic conductivities was the same ( $\times 10^{-12}$  m/s). This comparison highlighted the effi-  
478 ciency of the rearrangement of hydraulic conductive macropores ensuing as the smectite frac-  
479 tion swells upon its saturation. Further, it accounted for the difference in the performance of  
480 COX<sub>c</sub> and its mixture with MX80-bentonite.

481 As the values of hydraulic conductivity progressively decreased, it was hypothesized that  
482 the microstructure in COX<sub>c</sub>/ MX80-bentonite-mixture samples was still rearranging after more  
483 than one year of saturation, and that values of hydraulic conductivities were likely reflecting a  
484 short- or intermediate-term state. In order to corroborate the hypothesis, the kinetics of hydrau-  
485 lic conductivity experiments were compared to that of constant-volume swelling pressure ex-  
486 periments of Middelhoff et al. (2020). They performed those experiments on similar samples  
487 under comparable conditions and observed the establishment of constant swelling pressure after  
488 seven days of saturation. The different kinetics was attributed to the hydraulic gradient exceed-  
489 ing 500 m/m in constant-volume swelling pressure experiments. The higher hydraulic gradient  
490 involved higher rates of normalized inflow, thus a greater volume of solution for hydro-me-  
491 chanical processes was accessible in less time. This might account for an accelerated kinetics  
492 in constant-volume swelling pressure experiments. Nevertheless, it is recommendable to per-

493 form combined constant-volume swelling pressure/ constant-head hydraulic conductivity ex-  
494 periments in order to better understand the kinetics of swelling pressure build-up and swelling-  
495 induced pore closure and their coupling.

## 496 5.2 Impact of solution chemistry

497 The texture and microstructure of M-SS and M-AS were more affected by the saturation  
498 than by the solution chemistry. The solution chemistry, in particular that of the alkaline solution,  
499 had no impact neither on the shape of N<sub>2</sub>-gas sorption isotherms nor on SSA-values nor on their  
500 spatial distribution (e.g. Figure 5). Considerable textural and microstructural changes were ex-  
501 pected as the alkaline solution percolates the materials over time and dissolve the clay minerals  
502 therein. In turn, their dissolution alters the shape of mesopores and increases the fraction of  
503 macropores (Karnland et al., 2007; Cuisinier et al., 2008; Cuisinier et al., 2014). The impact of  
504 the solution chemistry must be considered to be highly time-dependent. The reaction kinetics  
505 appeared to be low under realistic conditions, and dissolution processes presumably did not  
506 come into effect, yet.

507 There was no considerable impact of the solution chemistry on the hydraulic conductivity  
508 behavior exhibited by M-W and M-SS. It might be attributable to the low ionic strength of the  
509 site solution ( $I_{SS} = 105$  mmol/L). According to the theories of diffuse double layers (DDL), the  
510 solution chemistry has an impact on the hydraulic conductivity behavior of smectite-based ma-  
511 terials, when diffuse double layers evolve in macropores and immobilize water molecules  
512 therein. The ion concentration in solution is inversely proportionally related to their layer thick-  
513 ness. An increase in hydraulic conductivity ensues as the ion concentration increases and, in  
514 turn, diffuse double layers diminish (e.g. Dixon, 2000; Villar, 2006; Castellanos et al., 2008).

515 In contrast, M-AS exhibited lowest values of hydraulic conductivity at the same normal-  
516 ized outflow of 0.6. This might be attributable to the clogging of hydraulic conductive  
517 macropores through swelling as well as precipitation of Ca(OH)<sub>2</sub>. The majority of pores in

518 M-AS were initially filled with water. Upon saturation, the pH-value of the alkaline solution  
519 dropped as it mixed with the pore water, and the consequent precipitation of  $\text{Ca}(\text{OH})_2$  intensi-  
520 fied the clogging of macropores.  $\text{Ca}(\text{OH})_2$  precipitated until the alkaline solution determined  
521 the pH-value of the pore solution, and dissolved then again. Since the precipitation of  $\text{Ca}(\text{OH})_2$   
522 changes the texture of materials, in particular their SSA-values, but  $\text{N}_2$ -gas sorption analyses  
523 revealed no changes, it can be hypothesized that  $\text{Ca}(\text{OH})_2$  already dissolved at that stage. An  
524 analyzes of the effluent and comparison of its  $\text{Ca}(\text{OH})_2$ -content to that of the influent can cor-  
525 roborate the hypothesis. Considering Middelhoff et al. (2020), the precipitation of  $\text{Ca}(\text{OH})_2$   
526 presumably has no impact on the evolution of swelling pressure, unlike on that of hydraulic  
527 conductivity.

528         Apart from the low reaction kinetics under imposed conditions, the low volume of pore  
529 solution exchanged might account for the apparently negligible impact of the solution chemis-  
530 try. As shown in Figure 3b, pore solution was exchanged less than once. Geochemical reactions,  
531 in particular dissolution and precipitation processes, appeared to not come into effect yet, de-  
532 spite the experiment duration of more than 300 days. The adoption of a different termination  
533 criteria is thus recommended that additionally considers the composition, ionic strength, and  
534 electric conductivity of the influent and effluent in order to predict the initiation of geochemical  
535 reactions in the course of the experiment more precisely. For instance, Jo et al. (2005) carried  
536 out long-term hydraulic conductivity experiments on geosynthetic clay liners. Values of hy-  
537 draulic conductivity were measured once hydraulic equilibrium established and once both hy-  
538 draulic and chemical equilibrium established. Unlike the former, the latter criteria was not met  
539 until the pore solution was exchanged several times. The comparison of results revealed an  
540 underestimation of the hydraulic conductivity by a factor of two when the termination criteria  
541 relied on the hydraulic equilibrium criteria exclusively. This also highlights the importance of  
542 volume of pore solution exchanged.

## 543 6 Conclusions

544 Crushed Callovo-Oxfordian claystone (COX<sub>c</sub>) and a mixture composed of 70% COX<sub>c</sub>  
545 and 30% MX80-bentonite in weight might be employed to backfill drifts and shafts of a future  
546 nuclear waste repository located in deep sedimentary rock formations. In addition to the swell-  
547 ing pressure, the hydraulic conductivity is one of the key parameters determining the perfor-  
548 mance of the backfill. This study aimed to understand the evolution of the hydraulic conductiv-  
549 ity by means of laboratory experiments, whose boundary conditions were believed to portray  
550 the real conditions in terms of compaction conditions, solution chemistry, temperature and hy-  
551 draulic gradient. Subsequently conducted microstructural and textural analysis allowed to relate  
552 the evolution of the hydraulic conductivity at the macroscale to changes at the microscale pos-  
553 sibly affected by the solution chemistry, in particular the pH-value. Following major conclu-  
554 sions can be drawn for COX<sub>c</sub> and its mixture with MX80-bentonite:

- 555 1. The microstructural analysis showed considerable microstructural rearrangements, which  
556 were related to closure of macropores triggered by material swelling upon saturation. The  
557 interpretation was consistent with the observations and the literature. The negligible im-  
558 pact of the solution chemistry was attributed to the low volume of exchanged pore solu-  
559 tion under imposed conditions.
- 560 2. In the case of COX<sub>c</sub> and the mixture, values of hydraulic conductivity were in good agree-  
561 ment with the literature. COX<sub>c</sub> exhibited stabilized values of hydraulic conductivity soon  
562 upon establishing steady state conditions. Conversely, values of hydraulic conductivity  
563 of the mixture progressively decreased in the course of the experiment. Considering the  
564 results of microstructural analysis, the closure of hydraulic conductive macropores  
565 through material swelling upon saturation likely accounted for the evolution of the hy-  
566 draulic conductivity on the one side and for the difference in the performance of COX<sub>c</sub>  
567 and the mixture on the other side. The duration of some experiments was longer than one



568 year and highlighted the low kinetics of geochemical reactions under the imposed condi-  
569 tions. Hence, the hydraulic conductivity appeared to be little affected by the solution  
570 chemistry within one year of experiment duration. In order to study the time-dependent  
571 impact of solution chemistry more precisely, it is of major interest to conduct experiments  
572 which involve the exchange of several volumes of pore solution.

573 This study revealed that the replacement of COX<sub>c</sub> by 30% MX80-bentonite in weight  
574 enhanced considerably the barrier functions of compacted backfill materials under realistic con-  
575 ditions in terms of their short- and intermediate-term hydraulic conductivity. The enhancement  
576 can be attributed to the more effective clogging of hydraulic conductive voids. However, im-  
577 portant questions arose while evaluating the experiments. For instance, it is still unclear how  
578 the hydraulic conductivity evolves under imposed conditions in long-term, particularly with  
579 regard to the time-dependent impact of the solution chemistry that must not be considered as  
580 negligible and of the consolidation of the backfill material induced by the convergence of the  
581 rock formation.

582           **Declaration of interest**

583           The authors wish to confirm that there are no known conflicts of interest associated with  
584 this publication and there has been no significant financial support for this work that could have  
585 influenced its outcome.

586           **Funding**

587           The work presented in this paper has been carried out during the preparation of the PhD  
588 thesis of the first author, which is funded by Andra (France), the French agency in charge of  
589 the management and disposal of nuclear waste.

590           **Acknowledgement**

591           The authors thank Dr. F. Claret of BRGM and Dr. G. Armand of Andra for fruitful dis-  
592 cussions that helped to improve this article. Moreover, the authors gratefully thank the two  
593 anonymous reviewers for their rigorous revisions.

594

595 7 References

- 596 Alonso, E.E., Gens, A., Whight, D.W., 1987. General Report, in: Groundwater effects in ge-  
597 otechnical engineering. Ninth european conference on soil mechanics and foundation en-  
598 gineering, Dublin. 31.08. - 03.09. A. A. Balkema, Rotterdam, Brookfield, pp. 1087–1146.
- 599 ANDRA, 2005. Dossier 2005 Argile Synthesis: Evaluation of the feasibility of a geological  
600 repository in an argillaceous formation. Meuse/ Haute-Marne site. Collection les Rap-  
601 ports. Agence nationale pour la gestion des déchets radioactifs, Châtenay-Malabry,  
602 1497 pp.
- 603 Burland, J.B., 1990. On the compressibility and shear strength of natural clays. Géotechnique  
604 40, 329–378.
- 605 Castellanos, E., Villar, M.V., Romero, E., Lloret, A., Gens, A., 2008. Chemical impact on the  
606 hydro-mechanical behaviour of high-density FEBEX bentonite. Physics and Chemistry of  
607 the Earth, Parts A/B/C 33, S516-S526.
- 608 Chen, F.H., 1988. Foundations on expansive soils. Elsevier science pub, Amsterdam, New  
609 York, 1463 pp.
- 610 Conil, N., Talandier, J., Djizanne, H., La Vaissière, R. de, Righini-Waz, C., Auvray, C., Mor-  
611 lot, C., Armand, G., 2018. How rock samples can be representative of in situ condition: A  
612 case study of Callovo-Oxfordian claystones. Journal of Rock Mechanics and Geotechnical  
613 Engineering 10, 613–623.
- 614 Cuevas, J., 2005. Geochemical reactions in FEBEX bentonite. In: Michau, N. (Ed.)  
615 ECOCLAY II - Effects of cement on clay barrier performance. Phase II. Final report,  
616 pp. 105–117.

617 Cuisinier, O., Deneele, D., Masrouri, F., Abdallah, A., Conil, N., 2014. Impact of high-pH  
618 fluid circulation on long term hydromechanical behaviour and microstructure of com-  
619 pacted clay from the laboratory of Meuse-Haute Marne (France). *Applied Clay Science*  
620 88-89, 1–9.

621 Cuisinier, O., Laloui, L., 2004. Fabric evolution during hydromechanical loading of a com-  
622 pacted silt. *International Journal for Numerical and Analytical Methods in Geomechanics*  
623 28, 483–499.

624 Cuisinier, O., Masrouri, F., Pelletier, M., Villieras, F., Mosser-Ruck, R., 2008. Microstructure  
625 of a compacted soil submitted to an alkaline PLUME. *Applied Clay Science* 40, 159–170.

626 Delage, P., Marcial, D., Cui, Y.J., Ruiz, X., 2006. Ageing effects in a compacted bentonite: a  
627 microstructure approach. *Géotechnique* 56, 291–304.

628 Dixon, D.A., 2000. Porewater salinity and the development of swelling pressure in bentonite-  
629 based buffer and backfill materials 2000-04. POSIVA Oy, Helsinki, 51 pp. Accessed 27  
630 October 2019.

631 Dixon, D.A., Graham, J., Gray, M.N., 1999. Hydraulic conductivity of clays in confined tests  
632 under low hydraulic gradients. *Canadian Geotechnical Journal* 36, 815–825.

633 Elert, K., Pardo, E., Rodriguez-Navarro, C., 2015. Mineralogical Evolution of Di- and Trioc-  
634 tahedral Smectites in Highly Alkaline Environments. *Clays and Clay Minerals* 63, 414–  
635 431.

636 Fernández, R., Ruiz, A.I., Cuevas, J., 2014. The role of smectite composition on the hyper-  
637 alkaline alteration of bentonite. *Applied Clay Science* 95, 83–94.

638 Gaboreau, S., Lerouge, C., Dewonck, S., Linard, Y., Bourbon, X., Fialips, C.I., Mazurier, A.,  
639 Prêt, D., Borschneck, D., Montouillout, V., Gaucher, E., Claret, F., 2012. In-situ interac-  
640 tion of cement paste and shotcrete with claystones in a deep disposal context. *American*  
641 *Journal of Science* 312, 314–356.

642 Gaboreau, S., Prêt, D., Tinsseau, E., Claret, F., Pellegrini, D., Stammose, D., 2011. 15 years of  
643 in situ cement–argillite interaction from Tournemire URL: Characterisation of the multi-  
644 scale spatial heterogeneities of pore space evolution. *Applied Geochemistry* 26, 2159–  
645 2171.

646 Gaboreau, S., Robinet, J.-C., Prêt, D., 2016. Optimization of pore-network characterization of  
647 a compacted clay material by TEM and FIB/SEM imaging. *Microporous and Mesoporous*  
648 *Materials* 224, 116–128.

649 Gaucher, E., Robelin, C., Matray, J.M., Négrel, G., Gros, Y., Heitz, J., Vinsot, A., Rebours,  
650 H., Cassagnabère, A., Bouchet, A., 2004. ANDRA underground research laboratory: inter-  
651 pretation of the mineralogical and geochemical data acquired in the Callovian–Oxfordian  
652 formation by investigative drilling. *Physics and Chemistry of the Earth, Parts A/B/C* 29,  
653 55–77.

654 Gregg, S.J., Sing, K.S., 1982. Adsorption, surface area and porosity, 2nd ed. Academic Press,  
655 London, New York.

656 Herbert, H.-J., Kasbohm, J., Moog, H., Henning, K.-H., 2004. Long-term behaviour of the  
657 Wyoming bentonite MX-80 in high saline solutions. *Applied Clay Science* 26, 275–291.

658 Herbert, H.-J., Kasbohm, J., Sprenger, H., Fernández, A.M., Reichelt, C., 2008. Swelling  
659 pressures of MX-80 bentonite in solutions of different ionic strength. *Physics and Chemis-*  
660 *try of the Earth, Parts A/B/C* 33, S327-S342.

661 Hofmann, H., Bauer, A., Warr, L.N., 2004. Behavior of Smectite In Strong Salt Brines Under  
662 Conditions Relevant to the Disposal of Low- to Medium-grade Nuclear Waste. *Clays and*  
663 *Clay Minerals* 52, 14–24.

664 Huertas, F., Farias, J., Griffault, L., Leguey, S., Cuevas, J., Ramírez, S., Vigil de la Villa, R.,  
665 Cobena, J., Andrade, C., Alonso, M.C., Hidalgo, A., Parneix, J.C., Rassineux, F., Bouchet,

666 A., Meunier, A., Decarreau, S., Petit, S., Vieillard, P., 2000. ECOCLAY I - Effects of ce-  
667 ment on clay barrier performance. Final report. Off. for Off. Publ. of the Europ. Commu-  
668 nities, Luxembourg, 140 pp.

669 ISO, 2009. Particle size analysis: Laser diffraction methods.

670 Jo, H.Y., Benson, C.H., Shackelford, C.D., Lee, J.-M., Edil, T.B., 2005. Long-Term Hydraul-  
671 ic Conductivity of a Geosynthetic Clay Liner Permeated with Inorganic Salt Solutions. *J.*  
672 *Geotech. Geoenviron. Eng.* 131, 405–417.

673 Juang, C.H., Holtz, R.D., 1986. A probabilistic permeability model and the pore size density  
674 function. *International Journal for Numerical and Analytical Methods in Geomechanics*  
675 10, 543–553.

676 Karnland, O., Olsson, S., Nilsson, U., Sellin, P., 2007. Experimentally determined swelling  
677 pressures and geochemical interactions of compacted Wyoming bentonite with highly al-  
678 kaline solutions. *Physics and Chemistry of the Earth, Parts A/B/C* 32, 275–286.

679 Komine, H., 2004. Simplified evaluation on hydraulic conductivities of sand–bentonite mix-  
680 ture backfill. *Applied Clay Science* 26, 13–19.

681 Komine, H., 2010. Predicting hydraulic conductivity of sand–bentonite mixture backfill be-  
682 fore and after swelling deformation for underground disposal of radioactive wastes. *Engi-*  
683 *neering Geology* 114, 123–134.

684 Krauskopf, K.B., 1956. Dissolution and precipitation of silica at low temperatures. *Geo-*  
685 *chemica et Cosmochemica Acta* 10, 1–26.

686 Lippens, B., Boer, J.H. de, 1965. Studies on pore systems in catalysts V. The t method. *Jour-*  
687 *nal of Catalysis* 4, 319–323.

688 Lloret, A., Villar, M.V., 2007. Advances on the knowledge of the thermo-hydro-mechanical  
689 behaviour of heavily compacted “FEBEX” bentonite. *Physics and Chemistry of the Earth,*  
690 *Parts A/B/C* 32, 701–715.

691 Mata, C., 2003. Hydraulic behavior of bentonite based mixtures in engineered barriers: The  
692 backfill and plug test at the Aespoe HRL (Sweden). PhD Thesis, Barcelona, 280 pp.

693 Mata, C., Ledesma, A., 2003. Permeability of a bentonite-crushed granite rock mixture using  
694 different experimental techniques. *Géotechnique* 53, 747–758.

695 Michau, N. (Ed.), 2005. ECOCLAY II - Effects of cement on clay barrier performance: Phase  
696 II. Final report, 378 pp.

697 Middelhoff, M., Cuisinier, O., Masrouri, F., Talandier, J., Conil, N., 2020. Combined impact  
698 of selected material properties and environmental conditions on the swelling pressure of  
699 compacted claystone/bentonite mixtures. *Applied Clay Science* 184, 105389.

700 Molinero-Guerra, A., Delage, P., Cui, Y.J., Mokni, N., Tang, A.M., Aïmediou, P., Bernier, F.,  
701 Bornert, M., 2020. Water-retention properties and microstructure changes of a bentonite  
702 pellet upon wetting/drying; application to radioactive waste disposal. *Géotechnique* 70,  
703 199–209.

704 Norrish, K., 1954. The swelling of montmorillonite. *Discuss. Faraday Soc.* 18, 120.

705 Orsini, L., Remy, J.C., 1976. Utilisation du chlorure de cobaltihexammine pour la détermina-  
706 tion simultanée de la capacité d'échange et des bases échangeables des sols. *Bulletin de*  
707 *l'AFES Science du Sol* 4, 269–275.

708 Pusch, R., Zwahr, H., Gerber, R., Schomburg, J., 2003. Interaction of cement and smectitic  
709 clay—theory and practice. *Applied Clay Science* 23, 203–210.

710 Ramírez, S., Vieillard, P., Bouchet, A., Cassagnabère, A., Meunier, A., Jacquot, E., 2005. Al-  
711 teration of the Callovo–Oxfordian clay from Meuse-Haute Marne underground laboratory  
712 (France) by alkaline solution. I. A XRD and CEC study. *Applied Geochemistry* 20, 89–99.

713 Robinet, J.-C., Tyri, D., Djeran-Maigre, I., 2021. Hydro-mechanical response of crushed ar-  
714 gillite and bentonite mixtures as sealing material. *Engineering Geology* 288, 106140.

715 Romero, E., 2013. A microstructural insight into compacted clayey soils and their hydraulic  
716 properties. *Engineering Geology* 165, 3–19.

717 Romero, E., Gens, A., Lloret, A., 1999. Water permeability, water retention and microstruc-  
718 ture of unsaturated compacted Boom clay. *Engineering Geology* 54, 117–127.

719 Seyedi, D.M., Armand, G., Noiret, A., 2017. “Transverse Action” – A model benchmark ex-  
720 ercise for numerical analysis of the Callovo-Oxfordian claystone hydromechanical re-  
721 sponse to excavation operations. *Computers and Geotechnics* 85, 287–305.

722 Tang, C.S., Tang, A.M., Cui, Y.J., Delage, P., Shi, B., 2010. The coupled hydro-mechanical  
723 behaviours of compacted crushed Callovo-Oxfordian argillite. *Journal of Rock Mechanics*  
724 *and Geotechnical Engineering*, 86–90.

725 Thommes, M., Kaneko, K., Neimark, A.V., Olivier, J.P., Rodriguez-Reinoso, F., Rouquerol,  
726 J., Sing, K.S., 2015. Physisorption of gases, with special reference to the evaluation of sur-  
727 face area and pore size distribution (IUPAC Technical Report). *Pure and Applied Chemis-*  
728 *try* 87, 1051–1069.

729 Tourchi, S., Vaunat, J., Gens, A., Bumbieler, F., Vu, M.-N., Armand, G., 2021. A full-scale in  
730 situ heating test in Callovo-Oxfordian claystone: observations, analysis and interpretation.  
731 *Computers and Geotechnics* 133, 104045.

732 Villar, M.V., 2006. Infiltration tests on a granite/bentonite mixture: Influence of water salin-  
733 ity. *Applied Clay Science* 31, 96–109.

734 Wang, Q., Cui, Y.J., Delage, P., Gatmiri, B., 2012. Experimental study on the swelling behav-  
735 iour of bentonite/claystone mixture. *Engineering Geology* 124, 59–66.

736 Ye, W.M., Zheng, Z.J., Chen, B., Chen, Y.G., Cui, Y.J., Wang, J., 2014. Effects of pH and  
737 temperature on the swelling pressure and hydraulic conductivity of compacted GMZ01  
738 bentonite. *Applied Clay Science* 101, 192–198.



- 739 Yven, B., Sammartino, S., Geraud, Y., Villieras, F., 2007. Mineralogy, texture and porosity of  
740 Callovo-Oxfordian argillites of the Meuse/ Haute-Marne region eastern Paris Basin). Bul-  
741 letin de la Societe Geologique de France, 73–90.
- 742 Zeng, Z., Cui, Y.J., Zhang, F., Conil, N., Talandier, J., 2019. Investigation of swelling pres-  
743 sure of bentonite/claystone mixture in the full range of bentonite fraction. Applied Clay  
744 Science 178, 105137.
- 745 Zhang, C.-L., 2021. Deformation and water/gas flow properties of claystone/bentonite mix-  
746 tures. Journal of Rock Mechanics and Geotechnical Engineering 13, 864–874.
- 747 Zhang, C.-L., Kröhn, K.-P., 2019. Sealing behaviour of crushed claystone–bentonite mixtures.  
748 Geomechanics for Energy and the Environment 17, 90–105.

Table 1: Physical and physico-chemical characteristics of COX<sub>c</sub>, MX80-bentonite and the mixture

	Initial water content	Liquid limit	Plastic limit	Specific gravity	Cation exchange cap.	Ext. specific surface area
	$w_{ini}$	$LL$	$PL$	$G_s$	CEC	SSA
	[%]	[%]	[%]	[-]	[meq/100g]	[m <sup>2</sup> /g]
COX <sub>c</sub>	5.4	37.3	24.9	2.68	22	37
Mixture	6.4	112.5	34.7	2.64	39	32

751 Table 2: Major compounds and properties of site solution and alkaline solution (Middelhoff et al., 2020)

	Na <sup>+</sup>	K <sup>+</sup>	Ca <sup>2+</sup>	Mg <sup>2+</sup>	Cl <sup>-</sup>	HCO <sub>3</sub> <sup>-</sup>	SO <sub>4</sub> <sup>2-</sup>	OH <sup>-</sup>	IS	pH
	[mmol/L]	[mmol/L]	[mmol/L]	[mmol/L]	[mmol/L]	[mmol/L]	[mmol/L]	[mmol/L]	[mmol/L]	[-]
SS	44.8	0.5	5.3	8.5	35.3	1.5	1.8	-	105	7.8
AS	22.1	8.0	19.0	-	30.1	-	-	38.1	87	12.5

SS: Site solution; AS: Alkaline solution; IS: Ionic strength

752

753 Table 3: Initial characteristics of employed samples

Material	Initial dry density $\rho_{d, ini}$ [Mg/m <sup>3</sup> ]	Initial water content $w_{ini}$ [%]	Initial void ratio $e_{ini}$ [-]	Initial porosity $n_{ini}$ [-]	Initial degree of saturation $S_r$ [-]	Initial suction $s$ [MPa]
COX <sub>c</sub>	1.95	13.2	0.37	0.27	0.96	1.5
Mixture	1.72	18.2	0.53	0.35	0.91	2.7

754

755 Table 4: Experiment program including hydraulic conductivity experiments, microstructural and textural analysis

Sample ID.	C-I	C-W	C-SS	C-AS	M-I	M-W	M-SS	M-AS
Material	COX <sub>c</sub>	COX <sub>c</sub>	COX <sub>c</sub>	COX <sub>c</sub>	Mixture	Mixture	Mixture	Mixture
Solution	-	Water	SS	AS	-	Water	SS	AS
Constant head experiment	-	✓	✓	✓	-	✓	✓	✓
Mercury Intrusion Porosimetry (MIP)	✓	-	-	-	✓	-	✓	✓
N <sub>2</sub> -gas sorption	✓	-	-	-	✓	-	✓	✓

✓: Experiment performed

757  
758

Table 5: Absolute and relative values of microstructural characteristics of top and bottom parts of C-I, M-I, M-SS and M-AS

Sample-ID.	Absolute					Relative		
	$n^*$	$e_{tot}$	$e_M$	$e_m$	$e_\mu$	$e_M/e_{tot}$	$e_m/e_{tot}$	$e_\mu/e_{tot}$
	[-]	[-]	[-]	[-]	[-]	[-]	[-]	[-]
C-I (T)	0.28	0.388	0.225	0.111	0.052	0.58	0.29	0.13
C-I (B)	0.27	0.368	0.209	0.112	0.047	0.57	0.30	0.13
M-I (T)	0.34	0.501	0.287	0.146	0.068	0.57	0.29	0.14
M-I (B)	0.37	0.591	0.386	0.143	0.062	0.65	0.24	0.10
M-SS (T)	0.30	0.435	0.254	0.158	0.023	0.58	0.36	0.05
M-SS (B)	0.32	0.470	0.261	0.150	0.059	0.56	0.32	0.13
M-AS (T)	0.29	0.399	0.236	0.150	0.013	0.59	0.38	0.03
M-AS (B)	0.29	0.406	0.238	0.157	0.011	0.59	0.39	0.03

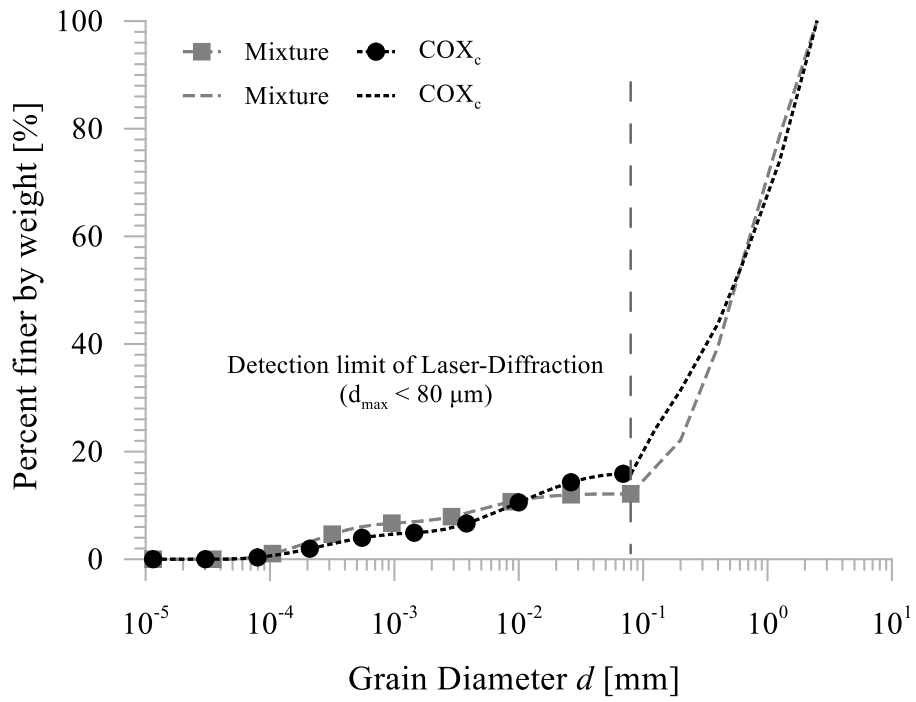
\*: measured in MIP-experiments

759

760 Table 6: SSA-values of different samples obtained by means of BET and  $t$ -plot

Sample	Samp. part	Height	BET			t-plot	
		h [mm]	$V_m^a$ [cm <sup>3</sup> /g]	$C^b$ [-]	$S_{Tot}^c$ [m <sup>2</sup> /g]	$V_{\mu pores}^d$ [cm <sup>3</sup> /g]	$S_{Tot}^c$ [m <sup>2</sup> /g]
C-I	Bottom	3	8.39	274	37	0.0029	37
	Middle	15	8.39	274	37	0.0029	37
	Top	27	8.39	274	37	0.0029	37
M-I	Bottom	3	7.43	431	32	0.0043	31
	Middle	15	7.43	431	32	0.0043	31
	Top	27	7.43	431	32	0.0043	31
M-SS	Bottom	3	7.44	331	33	0.0032	32
	Middle	15	7.37	875	32	0.0032	32
	Top	27	7.00	964	31	0.0052	29
M-AS	Bottom	3	7.36	435	32	0.0039	31
	Middle	15	7.23	697	32	0.0039	31
	Top	27	7.00	762	31	0.0046	29

<sup>a</sup>: Associated monolayer capacity; <sup>b</sup>: BET energy constant; <sup>c</sup>: Total specific surface area; <sup>d</sup>: Equivalent specific volume of micropores

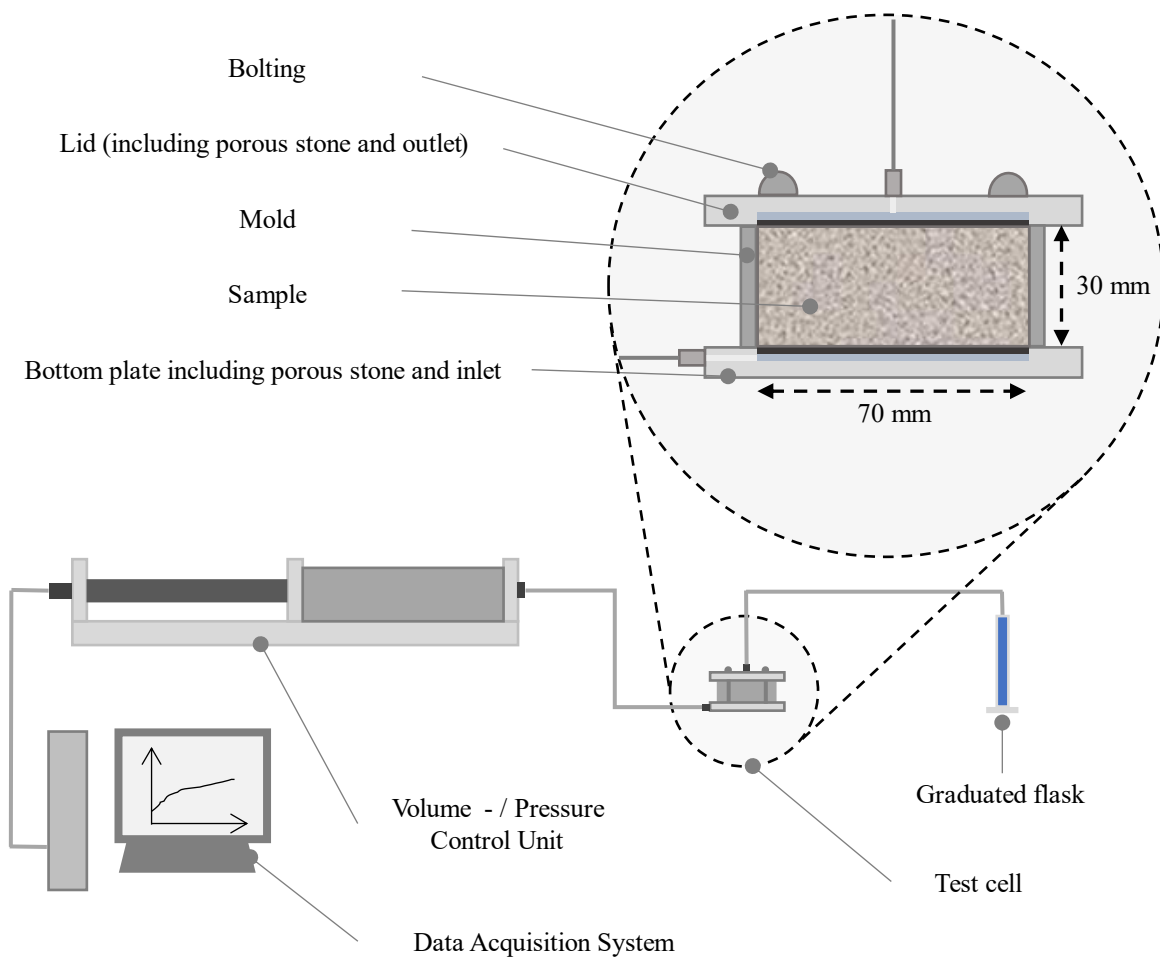


763

764 Figure 1: Grain size distribution curves of COX<sub>c</sub> and the mixture obtained by dry sieving and laser diffractometry  
 765 (Middelhoff et al., 2020)

766

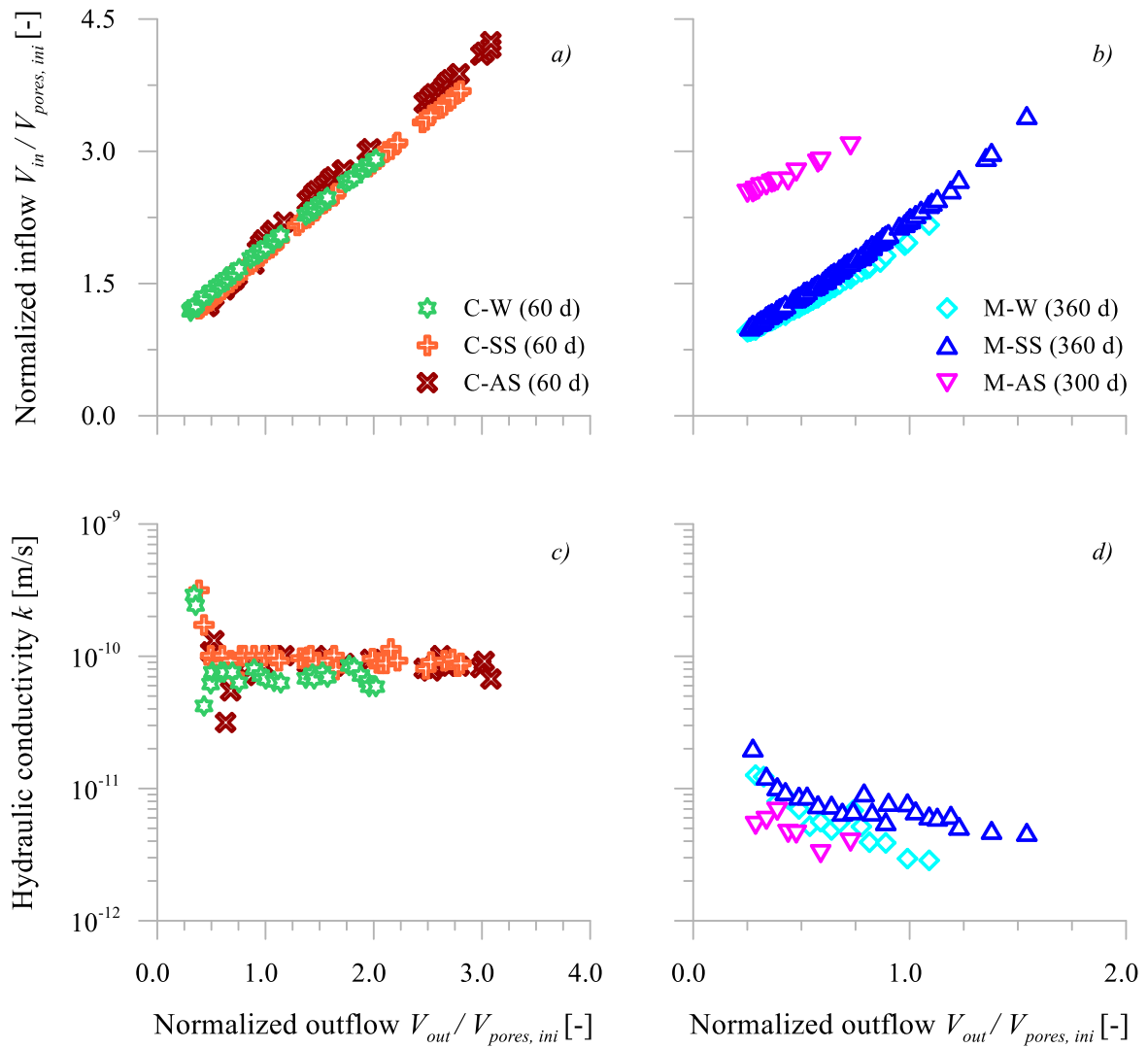




767

768 Figure 2: Setup of hydraulic conductivity experiments

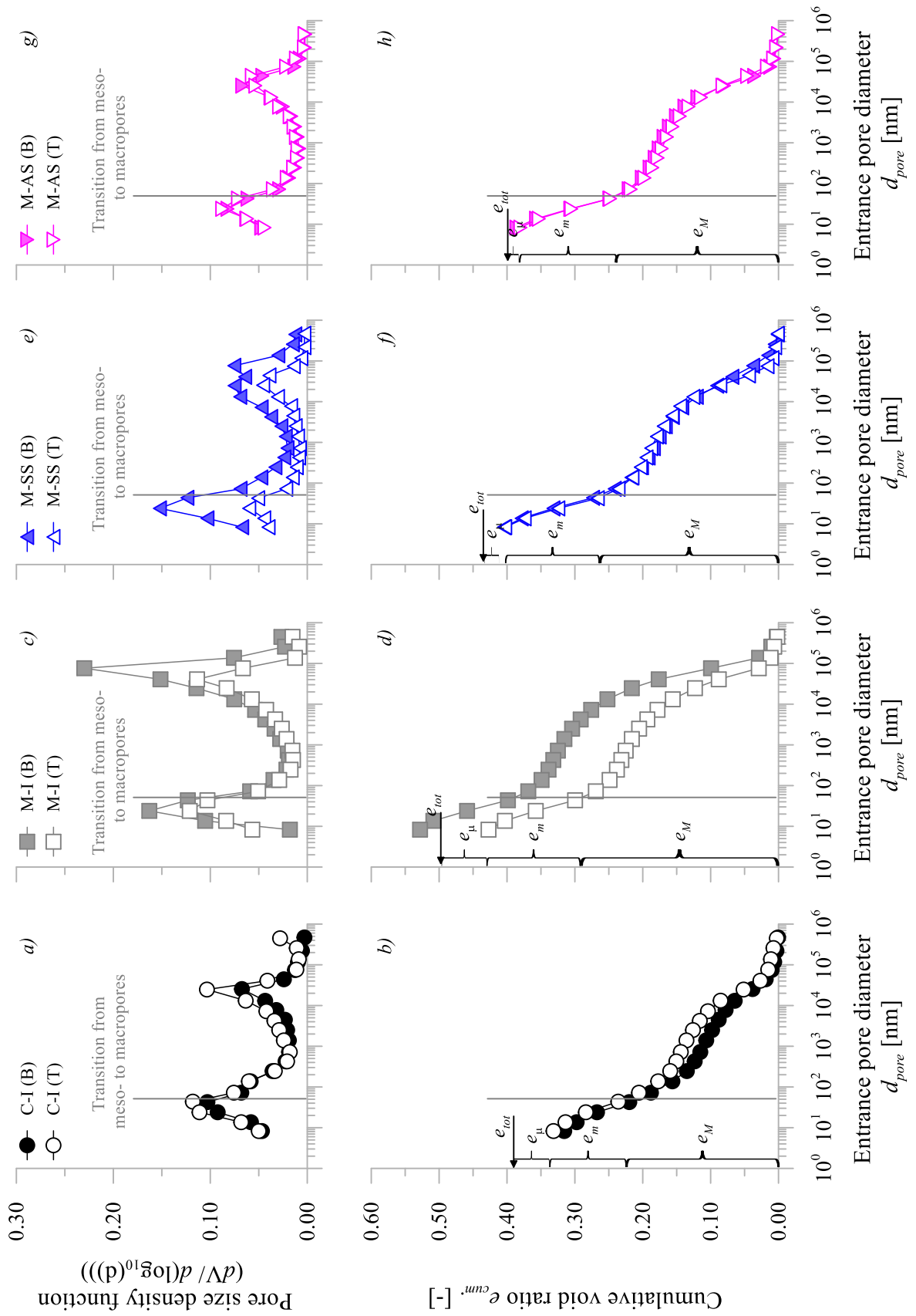
769



770

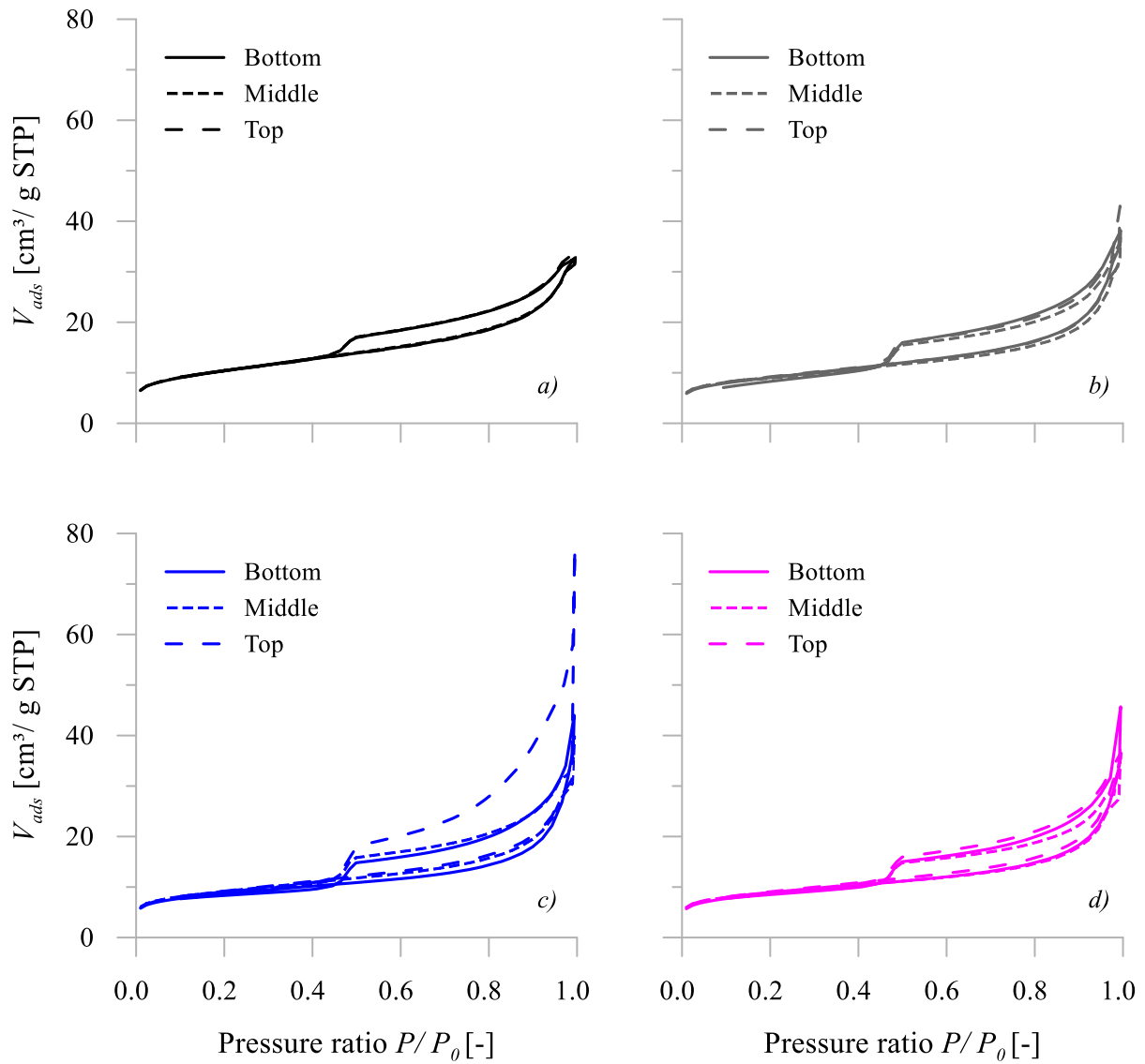
771 Figure 3: Evolution of the normalized inflow and the hydraulic conductivity of a, c) COX<sub>c</sub> ( $\rho_{d, ini} = 1.95 \text{ Mg/m}^3$ )  
 772 and b, d) the mixture ( $\rho_{d, ini} = 1.72 \text{ Mg/m}^3$ ) as function of the normalized outflow (saturated with water (-W), site  
 773 solution (-SS) and alkaline solution (-AS))

774



775

776 Figure 4: Results of mercury intrusion porosimetry (MIP) experiments conducted on the top and bottom parts of  
 777 samples C-I, M-I, M-SS and M-AS



778

779 Figure 5: Isotherms\* obtained by means of N<sub>2</sub>-sorption experiments conducted on the top (27 mm), middle  
 780 (15 mm) and bottom parts (3 mm) of samples C-I, M-I, M-SS and M-AS (\* Pressure ratio versus volume of gas  
 781 adsorbed ( $V_{ads}$ ) at standard pressure and temperature (SPT))